Chem Soc Rev

TUTORIAL REVIEW

View Article Online
View Journal | View Issue

Cite this: *Chem. Soc. Rev.*, 2015, **44**, 4501

Recent advances in magnetic nanoparticle-based multi-modal imaging

Tae-Hyun Shin, Youngseon Choi, Soojin Kim and Jinwoo Cheon*

Received 18th October 2014

DOI: 10.1039/c4cs00345d

www.rsc.org/csr

Magnetic nanoparticles have been extensively explored as a versatile platform for magnetic resonance imaging (MRI) contrast agents due to their strong contrast enhancement effects together with the platform capability for multiple imaging modalities. In this tutorial review, we focus on recent progress in the use of magnetic nanoparticles for MRI contrast agents and multi-mode imaging agents such as T_1–T_2 MRI, MRI-optical, and MRI-radioisotopes. This review also highlights emerging magnetic imaging techniques such as magnetic particle imaging (MPI), magneto-motive ultrasound imaging (MMUS), and magneto-photoacoustic imaging (MPA).

Key learning points
(1) Basic principles of MRI and key design parameters for nanoparticle-based MRI contrast agents.
(2) Essentials of multi-modal imaging for enhanced sensitivity and accuracy of biomedical imaging.
(3) Emerging magnetic imaging techniques: (i) MPI, (ii) MMUS, and (iii) MPA.

1. Introduction

During the past few decades, scientific breakthroughs from physics, chemistry, engineering, and medicine have led to biomedical imaging techniques with high sensitivity and resolution, which aid in both the understanding of biological phenomena and the detection of diseases. Currently, the representative imaging modalities in either preclinical research or clinical settings are MRI, positron emission tomography (PET), computed tomography (CT), single-photon emission computed tomography (SPECT), optical fluorescence imaging, ultrasound (US) imaging, and photoacoustic (PA) imaging (Table 1).[1] Owing to the need for accurate imaging of small biological targets in complex environments, new trials in performance enhancements of imaging techniques are in progress. One of the methods under study is the concept of multi-modality to complement the weakness of a single imaging modality with the strengths of other imaging modalities.[2] Another strategy is the use of imaging agents to overcome inherent instrumental limitations, such as sensitivity or resolution of a particular imaging technique, and ultimately to enhance the accuracy of biomedical imaging.[3] In particular, magnetic nanoparticles have been serving as a platform for MRI contrast agents due to their tunable properties such as magnetism, size, and facile conjugation with biologically functional units (Fig. 1a).[4] For example, the magnetic parameters, such as saturation magnetization (m_s) that proportionally affects the MRI contrast, can be optimized *via* fine control of the size or the composition of the nanoparticles. In addition, their surface functionalization provides them with the ability to carry a wide range of imaging moieties, such as fluorescent molecules and radioisotopes, which makes nanoparticles useful in multi-modal imaging systems. The versatility of magnetic nanoparticles has indeed allowed them to become an important platform for multi-modal imaging applications, such as MRI-optical and MRI–PET/SPECT, which combines the advantages of each imaging modality to achieve highly accurate images (Fig. 1b).[3] Recently, magnetic nanoparticles have also been demonstrated for their utility in non-traditional multi-modal imaging techniques, such as MPI, MMUS, and MPA that employ magnetic nanoparticles as a source of the imaging signals (Fig. 1c).

Magnetic nanoparticle-based multi-modal imaging can be categorized into two different approaches (Fig. 1b and c). One utilizes magnetic nanoparticles conjugated with secondary imaging components. These nanoparticles are designed to induce adequate signals in multiple imaging modalities, which can have the desired high spatial resolution (*e.g.* MRI) and sensitivity (*e.g.* optical, PET, or SPECT). When these signals are combined in a complementary manner, the biological targets can be imaged with high accuracy. The other approach uses the inherent magnetic properties of magnetic nanoparticles as a source of multi-modal imaging signals

Department of Chemistry, Yonsei University, Seoul, 120-749, Korea.
E-mail: jcheon@yonsei.ac.kr

Table 1 Comparison of the representative imaging modalities

Imaging techniques	Signal measured	Spatial resolution	Sensitivity[a]	Penetration depth[a]	Preclinical use	Clinical use
MRI	Radio frequency waves	+++	+	+++	Yes	Yes
PET	γ-rays	+	+++	+++	Yes	Yes
SPECT	γ-rays	+	++	+++	Yes	Yes
Optical (FLI or BLI)	Visible to infrared light	+	++	+	Yes	No
MPI	Radio frequency waves	+	++	+++	Yes	No
US imaging	High frequency sound waves	++	+	+	Yes	Yes
PA imaging	High frequency sound waves	++	++	+	Yes	No

MRI, magnetic resonance imaging; PET, positron emission tomography; SPECT, single-photon emission computed tomography; FLI, fluorescence imaging; BLI, bioluminescence imaging; MPI, magnetic particle imaging; US, ultrasound; PA, photoacoustic. [a] Strength and weakness are given using a relative scale (+, poor; ++, good; +++, excellent).

without additional imaging moieties. With the advance of several new imaging techniques (*e.g.* MPI, MMUS, and MPA), which can directly visualize nanoparticles, the location of the magnetic nanoparticles can be determined.[5–7] These magnetic nanoparticle-based imaging techniques can be combined with conventional imaging techniques (*e.g.* MRI and US). The overlay of images from respective modalities provides accurate information on the distribution of the magnetic nanoparticles without the interference of background signals, which could ultimately lead to a higher diagnostic accuracy of diseases. These magnetic

Tae-Hyun Shin

Tae-Hyun Shin received his BS degree in chemistry from Yonsei University in 2010. He is currently a graduate student at Yonsei University. His research interest is on the design and construction of functionalized inorganic nanoparticles for molecular imaging.

Youngseon Choi

Youngseon Choi graduated from Hanyang University with a BS and MS and received his PhD in 2005 from the University of Michigan at Ann Arbor, where he studied the design, synthesis and biological applications of dendrimers under Professor James R. Baker, Jr. After post-doctoral training at the University of Florida at Gainseville, he moved to Institut Pasteur Korea, where he worked on biomedical applications of quantum dots. He is currently a Research Professor at the Center for Evolutionary Nanoparticles at Yonsei University.

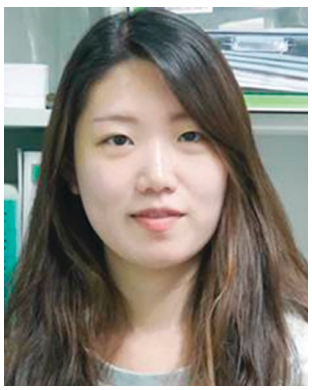

Soojin Kim

Soojin Kim received her BS degree in chemistry from Yonsei University in 2013. She is currently pursuing her PhD at Yonsei University. Her current research interest is on inorganic nanoparticles for MRI-based molecular imaging and biosensors.

Jinwoo Cheon

Jinwoo Cheon is the Horace G. Underwood Professor at Yonsei University and the director of the National Creative Research Initiative Center for Evolutionary Nanoparticles. He graduated from Yonsei University with a BS and received his PhD from the University of Illinois at Urbana-Champaign. After his postdoctoral training at U.C. Berkeley and UCLA, he joined KAIST. In 2002, he moved to Yonsei University. He is a recipient of many awards, including the POSCO Prize, Inchon Prize, and Song-gok Science Award. Currently, he is a senior editor of Accounts of Chemical Research and a fellow of the American Chemical Society and the Royal Society of Chemistry.

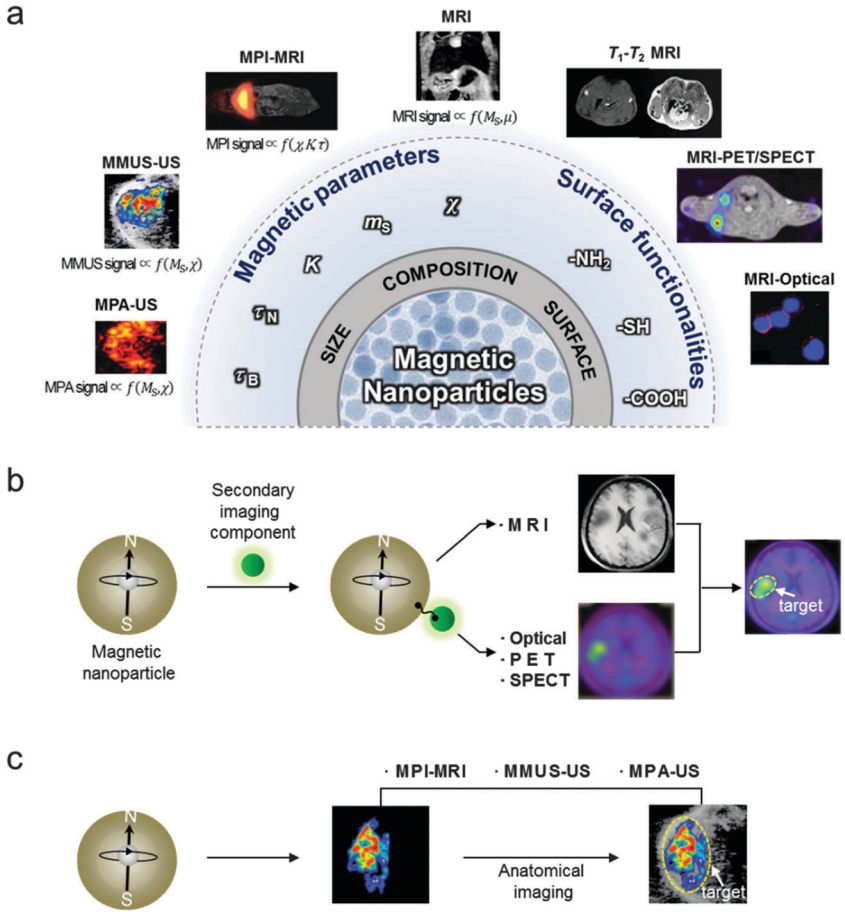

Fig. 1 Versatility of magnetic nanoparticles as a platform material for various imaging modalities. (a) The magnetic parameters (χ, magnetic susceptibility; m_s, saturation magnetization; K, anisotropy; τ_N, Néel relaxation time; τ_B, Brownian relaxation time) and surface functionalities of the magnetic nanoparticles are tuned *via* the size, composition, and surface chemistry of the nanoparticles. (b and c) Schematic illustrations of two different approaches of magnetic nanoparticle-assisted multi-modal imaging. (b) Magnetic nanoparticles combined with secondary imaging component (*e.g.* fluorescent tag or radioisotope) can generate imaging signals for multiple imaging modalities. These complementary signals allow the enhanced imaging accuracy of targets. (c) Magnetic nanoparticles are first located with non-traditional imaging techniques such as MPI, MMUS, or MPA. Subsequently, in combination of anatomy information provided by either MRI or US, nanoparticle imaging agents can visualize biological targets in the region of interest.

nanoparticle-based multi-modal imaging approaches are being actively pursued to improve the accuracy of cancer diagnosis, cardiovascular disease imaging, and cell tracking in regenerative medicine.

In this review, we discuss how magnetic nanoparticles can be designed to enhance the sensitivity of MRI and synergistically integrated with other imaging modalities to achieve high accuracy. To better explain the MRI contrast effects of magnetic nanoparticles, we first discuss the basic principles of MRI and the effects of various nanoscale parameters on MRI contrast enhancements. Then, the development of nanoparticle multi-modal imaging techniques such as T_1–T_2 MRI, MRI-optical, and MRI–PET/SPECT dual-modal imaging will be discussed. Finally, we highlight recent demonstrations of magnetic nanoparticles as imaging agents for newly emerging multi-modal imaging techniques such as MPI, MMUS, and MPA.

2. Magnetic nanoparticles for MR imaging

Among a number of clinically available imaging techniques, MRI is considered one of the foremost diagnostic imaging tools because of its unique features, including high spatial resolution, strong soft tissue contrast, and no radiation risk.[8] Nonetheless, the inherently poor sensitivity of MRI remains a limitation for the accurate detection of small biological targets, such as tumors in early stage cancer or subtle anatomical changes. To address this sensitivity issue, magnetic nanoparticles have been used as MRI contrast agents. In this section, we discuss the basic principles of MRI and the development of nanoparticle-based MRI contrast agents.

2.1. Basic principles of MRI

Similar to nuclear magnetic resonance (NMR), MRI can utilize either ^{1}H, ^{11}B, ^{13}C, ^{19}F, or ^{31}P as a source of signal. Among these, water protons (^{1}H) are the most common source in the current clinical MRI technique.[8] Under an external magnetic field (B_0), proton nuclear spins are aligned parallel with the direction of B_0, which induces longitudinal magnetization. At the same time, the proton nuclear spins precess with a Larmor frequency of $\omega_0 = \gamma B_0$ (γ is gyromagnetic constant). When radiofrequency (RF) pulses of

ω_0 are applied, the proton nuclear spins are resonantly excited and aligned antiparallel with B_0, which generates transverse magnetization while decreasing the longitudinal magnetization. Upon removal of the RF pulse, the excited water protons relax to the ground state (*i.e.* align parallel with B_0) by emitting the energy gained from the RF pulse. This relaxation proceeds *via* two different processes: (i) T_1 longitudinal relaxation, which results in longitudinal magnetization recovery and (ii) T_2 transverse relaxation, which involves transverse magnetization decay originating from the loss of phase coherence and dephasing between the proton nuclear spins. MRI makes a record of these relaxation processes and then reconstructs them into gray scale images. MRI images can generally be categorized into two different imaging modes of T_1-weighted images and T_2-weighted images. For T_1-weighted MRI images, a faster T_1 relaxation rate (R_1, the inverse of T_1, s^{-1}) gives a brighter contrast, and for T_2-weighted MRI images, a faster T_2 relaxation rate (R_2, the inverse of T_2, s^{-1}) yields a darker contrast.

Typically, the different water proton densities and tumbling rates, which are some of the factors that affect the rate of water proton relaxation, cause various biological tissues and organs to show characteristically distinct MRI contrasts. However, when the contrast difference between the target tissue (*e.g.* pathological lesions) and the surroundings (*e.g.* normal tissues) is marginal, it is difficult to accurately detect the target region of interest (ROI). Thus, MRI contrast agents that can accelerate the T_1 or T_2 relaxation rate in the ROI are used to increase the contrast between the pathological lesions and the normal tissues.

2.2. Magnetic nanoparticles as MRI contrast agents

MRI contrast agents are classified into T_2 or T_1 MRI contrast agents, depending on their relaxivity coefficients (r_2 or r_1, $mM^{-1}\ s^{-1}$), which are the terms that define the ability to accelerate relaxation rates (R_2 or R_1, s^{-1}).[4] To be an effective T_2 MRI contrast agent, a high r_2 value is a prerequisite. In comparison, T_1 MRI contrast agents need to have a high r_1 and a low r_2/r_1 ratio. Magnetic nanoparticles can serve as effective T_2 or T_1 MRI contrast agents because the facile tuning of the nanoparticle magnetism permits them to have optimized r_2, r_1 values and r_2/r_1 ratios.

For strong T_2 contrast effects, it is desirable for nanoparticles to have large magnetization values. Under an external magnetic field, magnetic nanoparticles are magnetized, and they subsequently generate induced magnetic fields, which cause local magnetic perturbations. Because the precession frequency (ω_0) of the water proton is determined by the strength of the external magnetic field, this inhomogeneity of the magnetic field causes proton nuclear spins to precess at different frequencies. Consequently, the dephasing process of the proton nuclear spins is accelerated with a faster T_2 relaxation process. According to outer-sphere spin–spin relaxation approximation, the relationship between the magnetization and the T_2 relaxation rate (R_2) is described by eqn (1)

$$R_2 = \frac{1}{T_2} = \frac{256\pi^2\gamma^2}{405} {m_s}^2 V \times \frac{r^2}{D\left(1+\frac{L}{r}\right)} \quad (1)$$

where γ is the gyromagnetic ratio of the protons, m_s is the saturation magnetization of the nanoparticle, V is the nanoparticle volume fraction, r is the radius of the magnetic nanoparticle, D is the diffusion coefficient of the water molecules, and L is the thickness of the surface coating.[9] According to eqn (1), an R_2 is directly proportional to the square of m_s. Given that the magnetic properties of the nanoparticles can be easily tuned by controlling the physicochemical parameters, such as size and composition, it is possible to develop magnetic nanoparticles with large m_s values to attain high T_2 contrast effects.

In contrast, T_1 contrast effects arise from the magnetically disordered spin layers at the surfaces of the magnetic nanoparticles. The metal ions at the nanoparticle surface have various numbers of unpaired electrons (*e.g.* 5 unpaired electrons for Fe^{3+}) that effectively accelerate the T_1 relaxation process.[10] However, high magnetization of magnetic nanoparticles with high r_2 and r_2/r_1 values is not suitable for T_1 contrast agents. Therefore, increasing the portion of canted surface spins of nanoparticles by decreasing the size of the nanoparticles is devised to produce a large r_1 while decreasing r_2 and r_2/r_1 values. Theoretical investigations indicate that strong T_1 contrast effects can be achieved when the sizes of the magnetic nanoparticles are smaller than 10 nm.[11]

2.3. Effects of magnetic nanoparticles on the MRI signal

2.3.1. Size. The size of nanoparticles can greatly influence the MRI contrast effects. According to theoretical studies about nanoparticle size effects on T_2 relaxivity, there are three different size regimes – the motional average regime (MAR), the static dephasing regime (SDR), and the echo-limiting regime (ELR).[12] With the increasing size of nanoparticles, R_2 increases in the so-called MAR and reaches its maximum plateau (SDR). A further size increase results in a decrease of R_2 (ELR). Although nanoparticles in the SDR have the highest R_2, the size of magnetic nanoparticles used for MRI applications commonly falls within the MAR because nanoparticles in the SDR often suffer from uncontrollable aggregation facilitated by strong ferromagnetic dipolar interactions.

The saturation magnetization (m_s) of nanoparticles proportionally increases with the size of the magnetic nanoparticles (Fig. 2a and b), as described in eqn (2)

$$m_s = M_s[(r-d)/r]^3 \quad (2)$$

where M_s is the saturation magnetization of the bulk, r is the radius of the nanoparticle, and d is the thickness of the disordered surface spin layer.[4] Thus, T_2 contrast effects in the MAR can be enhanced by increasing the sizes of the nanoparticles (see eqn (1) in Section 2.2). A systematic investigation of the size effects on the T_2 contrast enhancement is demonstrated for iron oxide nanoparticles with sizes of 4 to 6, 9, and 12 nm (Fig. 2c).[13] As the nanoparticle size increases, the m_s values increase from 25 to 43, 80, and 102 emu g^{-1} (Fe), resulting in the increment of the T_2 relaxivity coefficient (r_2) up to 218 $mM^{-1}\ s^{-1}$, which is approximately 2-fold higher than that of the representative iron oxide-based T_2 MRI contrast agent (*i.e.* Feridex®, r_2 = 108 $mM^{-1}\ s^{-1}$).[14]

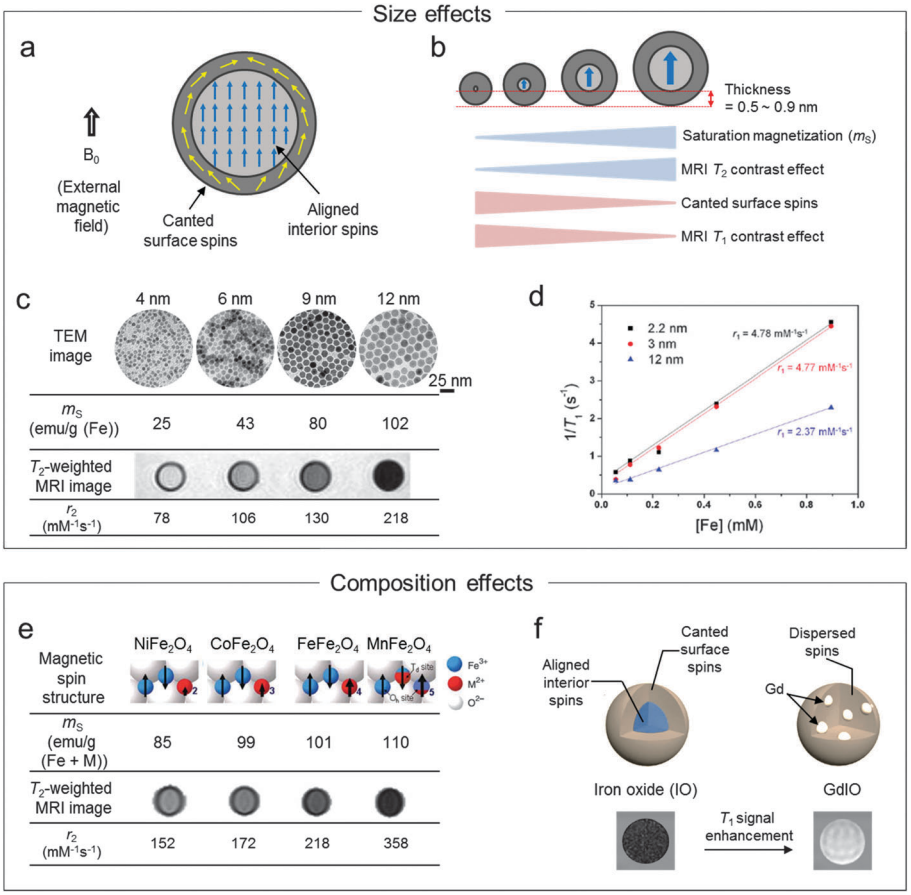

Fig. 2 Effects of the magnetic nanoparticles on MRI contrast enhancements. (a) Magnetic spins (aligned interior spins and canted surface spins) of nanoparticle under an external magnetic field (B_0). (b) Magnetic nanoparticle size *vs.* m_s, T_2 contrast effects, canted surface spins, and T_1 contrast effects. (c and d) The effects of the size on T_2 and T_1 contrast enhancements. (c) As the size of the nanoparticles increases from 4 nm to 12 nm, m_s and r_2 increase to 102 emu g^{-1} and 218 mM^{-1} s^{-1}, respectively. (d) The T_1 contrast effects (r_1) of extremely small size 3 nm iron oxide nanoparticles are *ca.* 2-fold higher than the 12 nm nanoparticles. (e and f) The effects of the composition on the T_2 and T_1 contrast enhancements. (e) Replacement of octahedral Fe^{2+} in ferrite nanoparticles with Mn^{2+} ($MnFe_2O_4$) results in *ca.* 1.5-fold increase in the r_2 value over Fe_3O_4. (f) The embedding of Gd species in iron oxide nanoparticles makes disruption of the interior spins into dispersed spin states with the resulting outcome of the enhanced T_1 contrast effects. (c) Reprinted with permission from ref. 13. Copyright 2005 American Chemical Society. (d) Reprinted with permission from ref. 10. Copyright 2011 American Chemical Society. (e) Reprinted with permission from Macmillan Publishers Ltd: ref. 20, copyright 2007. (f) Reprinted with permission from ref. 22. Copyright 2013 American Chemical Society.

Recently, there have been several reports to further increase the T_2 contrast effects by controlled clustering of magnetic nanoparticles to fit in the SDR.[15] The aggregates of magnetic nanoparticles can increase m_s and, thus, achieve a higher R_2. One of the methods for controlled nanocluster is encapsulating multiple magnetic nanoparticles in amphiphilic block-copolymer micelles.[15] For example, nanoclusters with a hydrodynamic size of 163 nm are prepared by enwrapping 7.4 nm iron oxide nanoparticles with poly(ethylene oxide-*co*-lactide) micelles. They show an r_2 of 229 mM^{-1} s^{-1}, which surpasses that of Feridex®. Alternatively, a template material, such as silica, has been tested to synthesize nanoclusters.[16] Typically, the r_2 value of the iron oxide nanoparticle cluster formed on the silica nanoparticle surface is higher than that of single iron oxide nanoparticles.

Such T_2 relaxivity changes induced by the clustering of the magnetic nanoparticles can be utilized to detect a wide range of biomarkers.[17,18] Termed as a magnetic relaxation switch (MRS), magnetic nanoparticles are modified with adequate functional molecules that can undergo assembly or disassembly in response to the presence of targets such as DNA, proteins, enzymes, and small molecules. Because most of the biomolecules are intrinsically low in magnetic susceptibility, an MRS can achieve high sensitivity with little interference from biological background.

T_1 contrast effects can be enhanced *via* reduction of the sizes of the nanoparticles (Fig. 2b), which is explained by the fact that the magnetically disordered spin layers on the nanoparticle surfaces make dominant contrast effects of the magnetic nanoparticles. The thickness of the spin canted surface layer is known to be 0.5–0.9 nm for iron oxide nanoparticles.[10] These size effects on the T_1 contrast enhancement have been investigated using extremely small iron oxide nanoparticles (ESIONs) with diameters of 2.2, 3, and 12 nm.[10] In the case of the 3 nm ESIONs, 93.6% of the spins are canted with a relatively high r_1 of 4.77 mM^{-1} s^{-1} (r_2/r_1 = 6.12), whereas 12 nm ESIONs with 38.6% of the canted

spins show an r_1 of 2.37 mM^{-1} s^{-1} (r_2/r_1 = 24.5) (Fig. 2d). The 3 nm ESIONs enhance the T_1 signal high enough to visualize MCF-7 cancer cells *in vitro*. Furthermore, the ESIONs provide sufficient sensitivity to obtain MRI images of small diameter (0.2 mm) blood vessels, demonstrating their potential for blood pool MR angiography. More recently, 5.5 nm iron oxide nanoparticles with a high r_1 value of 9.5 mM^{-1} s^{-1} and a low r_2/r_1 value of 2.97 are reported, where such strong T_1 contrast effects result from the small nanoparticle size facilitating diffusion of water molecules by the hydrophilic and compact PEG surface coating.[19]

2.3.2. Composition. The composition of the magnetic nanoparticles is another important parameter for MRI contrast effects. The magnetism of the nanoparticles can be easily tuned by introducing transition metal dopants. The metal dopant effects of metal ferrite nanoparticles have been studied by replacing Fe^{2+} in the octahedral sites of 12 nm nanoparticles with transition metal dopants such as Ni^{2+}, Co^{2+}, and Mn^{2+} (Fig. 2e).[20] The magnetism-engineered iron oxide (MEIO) nanoparticles (MFe_2O_4, M = Ni, Co, Fe, and Mn) exhibit saturation magnetization (m_s) values of 85, 99, 101, and 110 emu g^{-1} (Fe + M) and r_2 values of 152, 172, 218, and 358 mM^{-1} s^{-1}, respectively. Mn-doped MEIO nanoparticles with the highest r_2 value show highly sensitive MR imaging capability in small tumor xenografts (5 mm). The m_s values of the metal ferrite nanoparticles can be further increased upon addition of non-magnetic doping in the tetrahedral sites. When the Zn^{2+} doping level reaches 0.4 in $(Zn_xFe_{1-x})Fe_2O_4$, the resultant $(Zn_{0.4}Fe_{0.6})Fe_2O_4$ nanoparticles with an m_s value of 161 emu g^{-1} (Fe + Zn) exhibit an r_2 of 687 mM^{-1} s^{-1}.[21]

Similarly, this doping strategy is utilized to enhance T_1 contrast effects by doping rare-earth metals into ferrite nanoparticles. Gadolinium-embedded iron oxide (GdIO) nanoparticles are designed to disrupt the spin ordering of iron oxide (Fe_3O_4) (Fig. 2f).[22] Because Gd dopants influence the spin orientation of nanoparticles, not only the surface spins are canted but also the interior spins are magnetically disordered, which results in a low r_2/r_1 value. Thus, GdIO magnetic nanoparticles with a small size of 5 nm show higher T_1 contrast effects (r_1 = 7.85 mM^{-1} s^{-1} (Fe + Gd)) than iron oxide nanoparticles of the same size. GdIO exhibits a large T_1 signal enhancement in the cardiovascular system (*e.g.* heart) when intravenously injected into a mouse.

Despite these successful MRI contrast enhancements by the composition control, concerns over the biocompatibility of metallic components have been reported. Although iron oxide nanoparticles are generally known to be biocompatible,[23] other doping metals such as Gd have raised safety issues.[24] For example, Gd ions liberated from nanoparticles upon organ uptake cause toxic side effects such as nephrogenic systemic fibrosis (NSF).[24] One possible solution to minimize such issues is the fast excretion of nanoparticles *via* a renal clearance pathway, as demonstrated in the case of the 5 nm GdIO contrast agent.[22]

2.3.3. Shape. Recently, several studies have reported shape effects of the magnetic nanoparticles on MRI relaxivities.[25,26] According to eqn (1), the T_2 relaxivity is affected by both m_s and radius (r) of the nanoparticle. Therefore, for a certain m_s value, a much higher T_2 relaxivity can be possible by modulating r of the magnetic nanoparticle, which is largely shape dependent. For example, octapod Fe_3O_4 nanoparticles with an edge length of 30 nm have an r_2 value of 679 mM^{-1} s^{-1}, while 16 nm spherical Fe_3O_4 nanoparticles possessing a similar amount of Fe atoms and m_s show a much smaller r_2 value of 125 mM^{-1} s^{-1}.[25] The T_1 contrast effects can also be affected by the shape of nanoparticles. Fe_3O_4 nanoplates with iron-rich (111) exposed facets allow for increased interactions between surface Fe ions and water protons, resulting in strong T_1 contrast enhancement.[26] 8.8 nm thick Fe_3O_4 nanoplates exhibit an r_1 value of 38.11 mM^{-1} s^{-1}, which is more than 2-fold higher than that of 26 nm spherical Fe_3O_4 nanoparticles having an equivalent surface area. When the thickness of nanoplates is reduced to 4.8 nm, r_1 is further increased to 43.18 mM^{-1} s^{-1} due to the increased (111) surface area to volume ratio.

3. Magnetic nanoparticles for multi-modal imaging

In addition to the synthetic strategies such as size, composition, or shape control to improve MRI sensitivity, multi-modal imaging approaches have been examined to enhance both imaging sensitivity and accuracy. For example, imaging modalities such as PET can provide high sensitivity up to the femtomolar level of the biological targets of interest, while MRI can offer anatomical information with excellent resolution.[2] Thus, combining MRI with PET or optical modalities not only delivers high resolution and sensitivity but also provides more detailed and accurate imaging information than using either modality alone. For such a synergistic integration of multi-modalities, magnetic nanoparticles have served as a platform for the direct addition of fluorescent molecules or radioisotopes. In the following sections, we showcase recent developments in magnetic nanoparticles for T_1–T_2 MRI, MRI-optical, and MRI–PET/SPECT dual-modal imaging to show the versatility of magnetic nanoparticles as multi-mode imaging agents.

3.1. T_1–T_2 dual-mode MRI contrast agents

Conventional nanoparticle MRI contrast agents typically serve as single-mode contrast agents, generating either bright (T_1) or dark (T_2) signal enhancement. Frequently, even with the use of contrast agents several issues still need to be addressed to achieve the desired image quality. One of the challenging issues is how to minimize the artifact signals in MRI images. MRI artifacts are either bright or dark signals, which frequently originate from endogenous factors such as fat, calcification, hemorrhages, blood clots, and air.[23] These artifacts commonly found in disease lesions make it difficult to accurately identify the MRI signal coming from the contrast agents in the targets of interest.

To overcome such ambiguities and accurately interpret the MRI images, T_1–T_2 dual-mode contrast agents have been

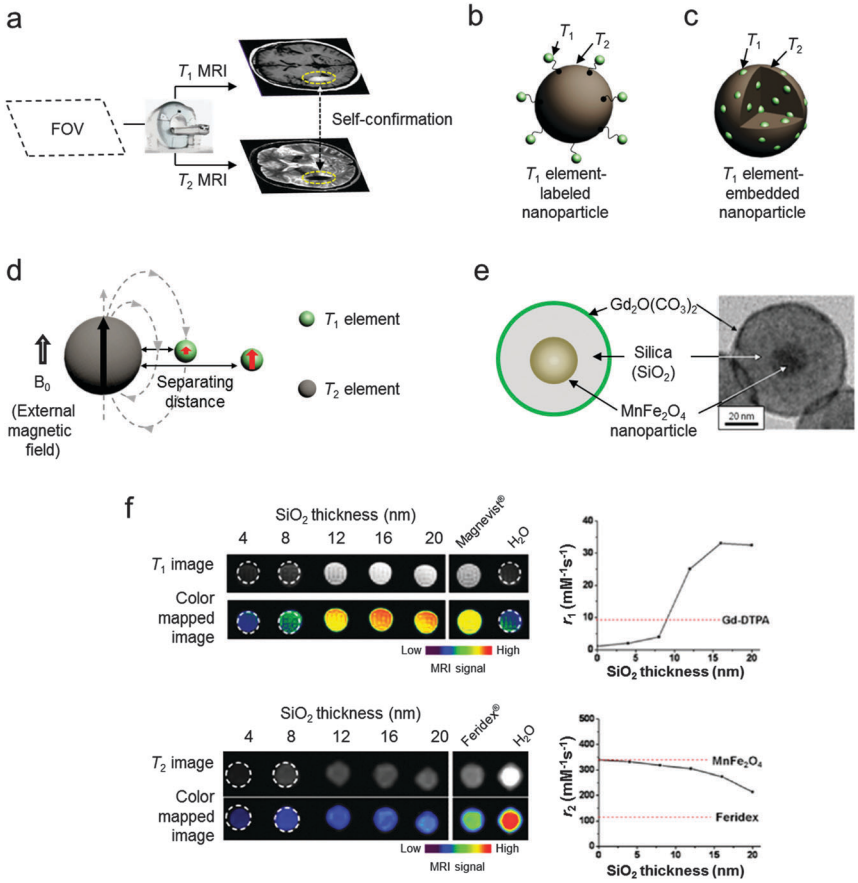

Fig. 3 Basics of T_1–T_2 MRI dual-modal imaging. (a) Conceptual sketch of dual-modal MRI. Two images from T_1 and T_2 scans of a field-of-view (FOV) are obtained using an MRI instrument. The T_1–T_2 dual-mode contrast agents provide simultaneously bright (T_1) and dark (T_2) contrast effects in the respective scans. An overlay of the concurrently high T_1 and T_2 signals can help distinguish biological targets from the surroundings. (b and c) Schematic illustrations of the two types of conjugated T_1–T_2 dual-mode contrast agents. (d) Distance dependent magnetic coupling between T_1 and T_2 elements. The magnetic spins of the T_1 element are perturbed by the T_2 element-induced magnetic field when two elements are located in close proximity. (e) The magnetically decoupled core–shell type T_1–T_2 dual-mode contrast agents (DMCAs) and the corresponding TEM image. (f) T_1 and T_2 MRI images of T_1–T_2 DMCAs with different thicknesses of the separating SiO_2 layer. Plots of r_1 and r_2 *vs.* SiO_2 thickness show that simultaneously high T_1 and T_2 contrast effects can be achieved with an optimal separating distance of 16 nm. (d–f) Reprinted with permission from ref. 14. Copyright 2010 American Chemical Society.

introduced. These dual-mode contrast agents provide complementary T_1-weighted and T_2-weighted MRI images that enable self-confirmation of the signals from the contrast agents (Fig. 3a). These multi-mode MRI contrast agents are designed for a single instrument and have some advantages. For example, there are no discrepancies in the penetration depth between T_1 and T_2 images and no image mismatch issues which can occasionally occur when moving a sample between different imaging instruments. These characteristics of T_1–T_2 dual-mode contrast agents can be achieved by exploiting the unique design concepts of nanoparticles.

3.1.1. Conjugated T_1–T_2 dual-mode contrast agents. A simple way to construct T_1–T_2 dual-mode contrast agents is the direct conjugation of T_1 elements (*e.g.* Gd- or Mn-based chelates) and T_2 elements (*e.g.* metal ferrite magnetic nanoparticles). To date, two different cases of conjugated T_1–T_2 systems have been reported. One is constructed by labeling T_1 signaling elements on magnetic nanoparticles (Fig. 3b).[27] Gd–DTPA (Magnevist®), a representative Gd chelate-based T_1 MRI contrast agent, is covalently attached to dopamine-coated iron oxide nanoparticles *via* isothiourea (SCN) linkage chemistry. The resultant Gd-labeled magnetite nanoparticles show both T_1 and T_2 contrast effects with an r_1 value of 11.17 mM^{-1} s^{-1} (Gd) and an r_2 value of 30.32 mM^{-1} s^{-1} (Fe), generating T_1–T_2 dual-mode MRI images *in vivo*.

Another type of conjugated system uses a design concept of embedding T_1 paramagnetic elements into T_2 magnetic nanoparticles (Fig. 3c).[28,29] For example, Gd_2O_3-embedded iron oxide nanoparticles with an overall size of 14 nm display high r_1 and r_2 values of 69.5 of mM^{-1} s^{-1} (Gd) and 146.5 mM^{-1} s^{-1} (Fe), respectively, leading to successful T_1–T_2 dual-modal MR imaging of hepatic tumor in mice.[28] Additionally, Mn-embedded iron oxide nanoparticles have r_1 and r_2 values of 18 mM^{-1} s^{-1} and 45.9 mM^{-1} s^{-1} (Fe + Mn), respectively.[29]

3.1.2. Magnetically decoupled T_1–T_2 dual-mode contrast agents (DMCAs). One of the possible ways to achieve concurrently high T_1 and T_2 contrast effects is the use of magnetically decoupled T_1–T_2 dual-mode contrast agents (DMCAs).[14,30] A non-magnetic separating layer (SiO_2) can be synthetically inserted between the T_2 contrast

magnetic nanoparticles (core) and the T_1 contrast materials (shell). Through fine control of the separation distance, the perturbation of the T_1 contrast effects by the T_2 contrast materials is modulated (Fig. 3d). For example, 15 nm Mn-doped iron oxide ($MnFe_2O_4$) nanoparticles are utilized as the T_2 contrast material in the core and $Gd_2O(CO_3)_2$ with a thickness of 1.5 nm is used as the T_1 contrast material in the shell (Fig. 3e).[14] The distance between the two materials is controlled using SiO_2 as a separating layer and a 16 nm separation is found to be optimal to ensure both high T_1 and T_2 contrast effects (Fig. 3f). The relaxivity coefficients (r_1 = 33.1 mM^{-1} s^{-1} (Gd) and r_2 = 274 mM^{-1} s^{-1} (Fe)) are approximately 2–3-fold higher than those of the conventional T_1 or T_2 contrast agents (Magnevist®, r_1 = 9.6 mM^{-1} s^{-1} and Feridex®, r_2 = 108 mM^{-1} s^{-1}). The generality of this design concept is further demonstrated by synthesizing various T_1–T_2 DMCAs with different combinations of magnetic materials for the core and shell.[30]

These T_1–T_2 DMCAs possess the ability to perform an AND logic gate algorithm which is useful for accurate interpretation of biological information by eliminating MRI artifacts.[14,30] An AND logic gate is designed to provide meaningful output only when both T_1 and T_2 signals are sufficiently high. Therefore, only the signals from T_1–T_2 DMCAs can be exclusively represented in images. This artifact filtering capability of T_1–T_2 DMCAs is shown in the MRI phantom control experiments with intentionally inserted T_1 or T_2 artifacts (Fig. 4a).[30] The T_1 and T_2 images of each phantom are processed using an AND logic gate algorithm to give an "MRI" AND image as the final image (Fig. 4b). The successful use of T_1–T_2 DMCAs in conjunction with the AND logic gate process is demonstrated *via in vivo* MRI stem cell tracking. T_1–T_2 DMCA-transfected neural stem cells are transplanted in a rat brain with a stroke. The stem cell tracking is visualized in the T_1–T_2 AND image with high accuracy (Fig. 4c).

T_1–T_2 DMCAs combined with AND logic gates can be a useful tool for enhancing the accuracy of MR imaging of small biological targets, including tumors in early stage cancer, lymph nodes, and cardiovascular plaques, where various MRI artifacts are present.

3.2. MRI-optical dual-mode imaging agents

One of the traditional approaches to complementing the low sensitivity of MRI is the addition of optical fluorescence modalities. Various types of MRI-optical probes have been reported, where optically active components are chemically or physically combined with magnetic nanoparticles.[16,31–34]

During early studies, MRI-optical dual-mode imaging agents have been constructed by conjugating fluorescent dyes to the surfaces of dextran-coated iron oxide nanoparticles.[31] In a similar approach, MRI-optical probes are prepared by conjugating cyanine 5.5 (Cy5.5, λ_{ex} = 649 nm, λ_{em} = 670 nm) to polymer-coated iron oxide nanoparticles (Fig. 5a).[32] The dual imaging capability is successfully demonstrated *in vivo* with nanomolar sensitivity. However, combining the fluorescent units with magnetic nanoparticles often suffers from fluorescence quenching, which originates from energy transfer between the fluorescent molecules

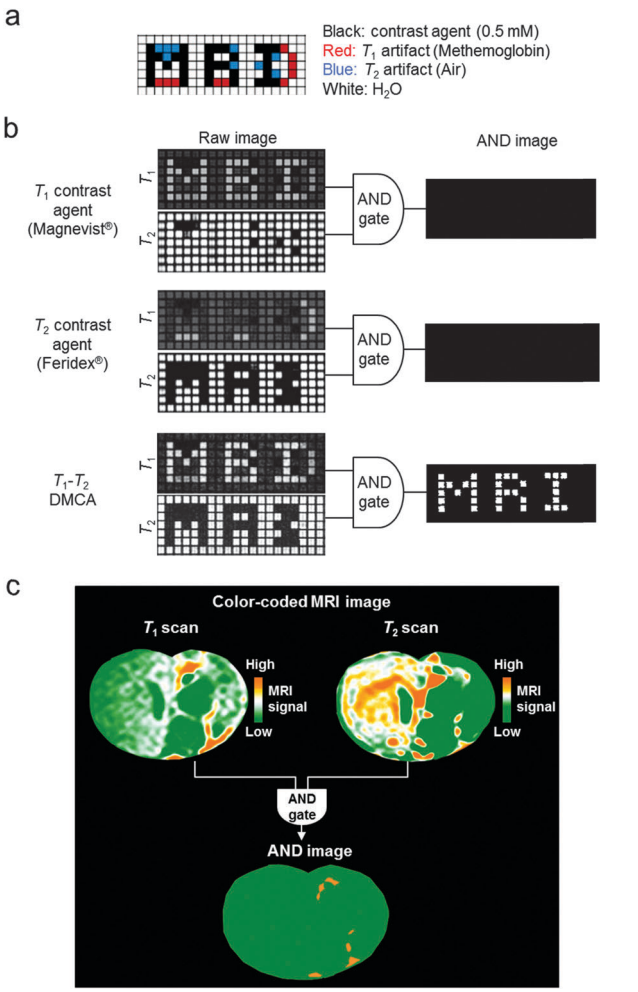

Fig. 4 MRI artifact filtering capability of T_1–T_2 DMCAs. (a) The design of MRI phantom plate containing contrast agents and artifacts. (b) T_1- and T_2-weighted raw images of phantoms and final AND images. After an AND logic gate process, the T_1–T_2 DMCAs show the character "MRI" with complete filtration of artifacts in the AND image, while the conventional single-mode MRI contrast agents (Magnevist® and Feridex®) exhibit no signal. (c) Color-coded MRI images of the T_1 and T_2 scans of a rat brain injected with T_1–T_2 DMCA-labeled stem cells. The orange signals in the AND image are the areas with simultaneously high T_1 and T_2 MRI contrasts, which indicate the locations of the migrated stem cells. Reprinted with permission from ref. 30. Copyright 2014 American Chemical Society.

and the magnetic nanoparticles. This quenching phenomenon is highly dependent on the distance between the fluorophores and the nanoparticles, which decreases as the distance increases. Thus, strategies such as the utilization of long chemical linkers or a thick silica surface coating layer have been implemented.[35] In a related approach, hybrid 'core–satellite' nanostructures are developed, where 30 nm dye-doped silica nanoparticles ('core') are decorated with multiple 9 nm iron oxide (Fe_3O_4) nanoparticles ('satellite') (Fig. 5b).[16] The core–satellite dual imaging agents exhibit a 3.4-fold increase in the T_2 MRI signal (r_2 = 397 mM^{-1} s^{-1}) compared with the individual nanoparticles (r_2 = 116 mM^{-1} s^{-1}) due to the nanoparticle clustering effects. The fluorescence signal is also enhanced by 1.7-fold compared with the directly dye-conjugated Fe_3O_4 nanoparticles. The 'core–satellite' MRI-optical dual-mode

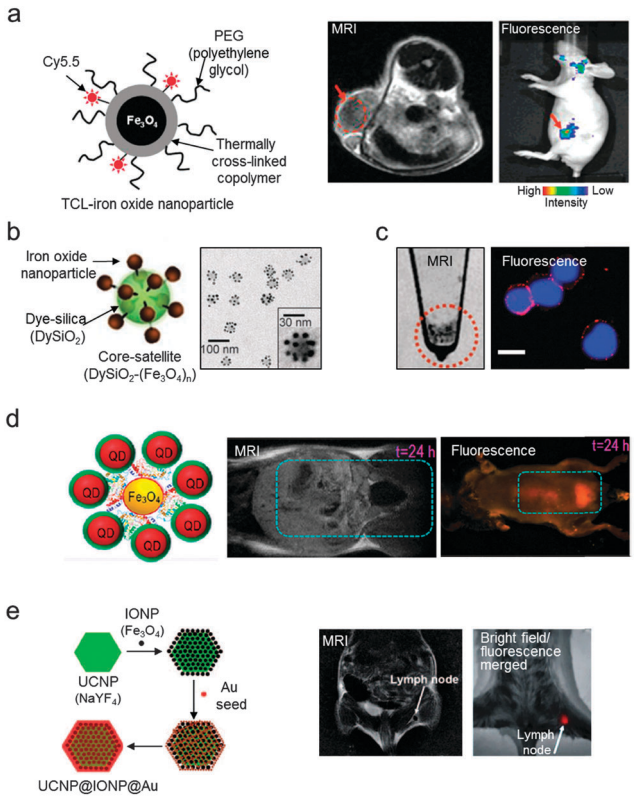

Fig. 5 Magnetic nanoparticle-based MRI-optical dual-mode imaging agents. (a) Iron oxide nanoparticles labeled with fluorescent dyes (Cy5.5) visualize tumors with high T_2 MRI signals (dark area in the red dotted circle) and fluorescence signals (red arrow). (b and c) 'Core–satellite' nanoparticles and their utilization in MRI-optical cancer cell imaging. (b) TEM image of 'core–satellite' nanoparticles composed of fluorescent dye-doped silica ($DySiO_2$) and multiple surrounding iron oxide (Fe_3O_4) nanoparticles. (c) MRI and fluorescence imaging of human neuroblastoma cells (CHP-134) using the 'core–satellite' nanoparticles. The red and blue colors in the fluorescence image indicate the nanoparticles and the nuclei of the cells, respectively. (d) Assembly of NIR QDs with Fe_3O_4 nanoparticles *via* the biotin–streptavidin interaction allows for the imaging of mouse bladder with both high T_2 MRI and NIR fluorescence signals. (e) UCNP-based nanoparticles composed of Fe_3O_4 and gold show the lymph node of a mouse *via* both T_2 MRI and fluorescence imaging (λ_{ex} = 980 nm, λ_{em} = 660 nm). (a) Reprinted with permission from ref. 32. Copyright 2007 American Chemical Society. (b and c) Reproduced from ref. 16 by permission of John Wiley & Sons Ltd. (d) Reprinted with permission from ref. 33. Copyright 2013 American Chemical Society. (e) Reproduced from ref. 34 by permission of John Wiley & Sons Ltd.

imaging agents enable sensitive imaging of sub-millimeter cellular clusters *via* both MRI and optical fluorescence imaging (Fig. 5c).

Optically active components other than fluorescent dyes include quantum dots (QDs). Using QDs, it is possible to ensure a high fluorescence signal owing to their exceptional photostability, large extinction coefficients, and tunable absorption properties. One example is the assembly of multiple near-infrared (NIR) emitting QDs on Fe_3O_4 nanoparticles (Fig. 5d).[33] NIR fluorescence offers deep tissue penetration capability, which allows high fluorescence sensitivity in deeply located organs such as the bladder. More recently, MRI-optical probes utilize NIR-to-visible upconversion nanoparticles (UCNPs) composed of lanthanide-doped rare-earth elements (Fig. 5e).[34] UCNPs are known to possess high photostability, a narrow emission peak, and a deeper penetration depth. The use of NIR light as an excitation source prevents autofluorescence in UCNP-based optical imaging, which frequently arises from endogenous aromatic amino acid molecules (*e.g.* tryptophan, tyrosine, and phenylalanine) when short-wavelength (*e.g.* ultraviolet) radiation is used as an excitation source.

3.3. MRI–PET/SPECT dual-mode imaging agents

Another important multi-modal imaging system has been achieved *via* the combination of radioisotope-based imaging techniques (*e.g.* PET or SPECT) with MRI. These nuclear imaging techniques utilize gamma-rays emitted from decaying radioisotopes (*e.g.* ^{18}F, ^{64}Cu, ^{68}Ga, and ^{124}I for PET and ^{99m}Tc, ^{111}In, and ^{131}I for SPECT). Generally, they offer high sensitivity, but have the limitation of relatively poor spatial resolution.[2] Therefore, a combined MRI and PET/SPECT dual-modal system can provide highly resolved tomographic images along with strong sensitivity, leading to accurate determination of quantitative biological information, such as *in vivo* biodistribution and pharmacokinetics, particularly in deep tissues.[19,36–39]

For the construction of MRI–PET/SPECT dual-mode imaging agents, magnetic nanoparticles have been modified with radioisotopes *via* chemical conjugation. One example is ^{124}I linking *via* tyrosine residues of serum albumin coated on Mn-doped ferrite nanoparticles (Fig. 6a).[36] The resultant MRI–PET dual imaging agents provide highly sensitive signals in both MRI and PET images. In an MRI–PET fused image, the two signals accurately delineate the different types of small sentinel lymph nodes of only a few millimeters in diameter. Another MRI–PET dual-mode imaging agent utilizes a macrocyclic chelating agent, DOTA (1,4,7,10-tetraazacyclododecane-*N*,*N*′,*N*″,*N*‴-tetraacetic acid), for radioisotope (^{64}Cu) labeling and an arginine–glycine–aspartic acid (RGD) peptide for selective targeting of tumor integrin $\alpha_v\beta_3$.[37] The conjugation of these functional moieties on polyaspartic acid-coated Fe_3O_4 nanoparticles allows *in vivo* targeted imaging of tumor xenografts by using both MRI and PET. Several robust radioisotope labeling strategies have also been developed. One example is the use of a bifunctional molecule composed of dithiocarbamate (DTC) and bisphosphonate (BP), which effectively chelates the radioisotope (^{64}Cu) and simultaneously binds to the surfaces of magnetic nanoparticles (Endorem®), respectively (Fig. 6b).[38] The final complex shows high stability under physiological conditions. The strong nanoparticle binding nature of BP can also be used to label radioisotopes for SPECT (Fig. 6c).[19] By using the ^{99m}Tc modified BP that binds irreversibly to the surface of iron oxide nanoparticles, an MRI–SPECT dual-mode agent with high radiolabel stability is obtained. Another example is the chelator-free labeling of arsenic (As), which has four positron emitting radioisotopes (*As; * = 70, 71, 72, and 74) (Fig. 6d).[39] Arsenic can be effectively labeled with magnetite by forming highly stable As complexes that occupy vacant tetrahedral sites of iron oxide. The dual imaging capabilities of

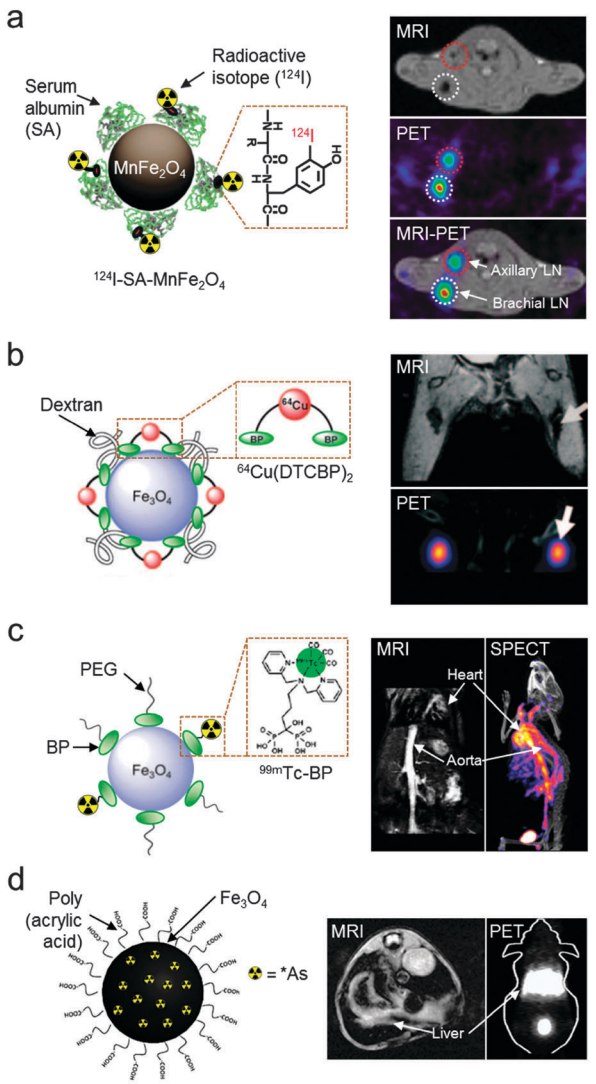

Fig. 6 MRI–PET/SPECT dual-mode imaging agents with a magnetic nanoparticle platform. (a) Radioisotope-labeled Mn-doped ferrite nanoparticles (^{124}I–SA–$MnFe_2O_4$) delineate the sentinel lymph nodes (axillary and brachial lymph nodes) with adequate PET signals and the anatomical MRI image. (b) Fe_3O_4 nanoparticles, which are labeled with radioisotope (^{64}Cu) chelator molecules (DTCBP) enable detection of popliteal lymph nodes with both MRI and PET signals (white arrows). (c) ^{99m}Tc-labeled Fe_3O_4 nanoparticles for MRI–SPECT dual-modal imaging. Cardiovascular organs such as the heart and aorta are visualized in MRI and SPECT images. (d) Arsenic (As)-labeled iron oxide nanoparticles *via* a chelator-free synthetic route and their application in MRI and PET dual-modal imaging of liver (white arrows). (a, b, and d) Reproduced from ref. 36, 38, and 39 by permission of John Wiley & Sons Ltd. (c) Reprinted with permission from ref. 19. Copyright 2012 American Chemical Society.

those MRI–PET/SPECT imaging agents are successfully demonstrated *in vivo* imaging studies where lymph nodes (Fig. 6b), cardiovascular organs (Fig. 6c), and the liver (Fig. 6d) are detected with high sensitivity. In particular, the use of dual-mode imaging agents with the integration of MRI and PET/SPECT plays an important role as an imaging platform in highly sensitive and high resolution imaging *in vivo*.

4. Magnetic nanoparticle-based non-traditional multi-modal imaging

In addition to the methods described above, during the past decade, magnetic nanoparticles have expanded their versatility in emerging multi-modal imaging techniques. Some examples are (i) magnetic particle imaging (MPI), (ii) magneto-motive ultrasound imaging (MMUS), and (iii) magneto-photoacoustic imaging (MPA). In conjunction with traditional imaging modalities (*e.g.* MRI and ultrasound (US) imaging) that provide anatomical information, new imaging modalities can be utilized to determine the location of magnetic nanoparticles in biological targets. Currently, MPI is combined with MRI, while MMUS and MPA are fused with US imaging. Because these new multi-modal imaging techniques all use magnetic nanoparticles as tracers, it is possible to achieve multi-modal imaging using only magnetic nanoparticles, without the need of tracers such as fluorescent molecules or radioisotopes. In the following sections, we will discuss the basic concepts of new multi-modal imaging techniques. The design considerations of magnetic nanoparticles for enhancing the image performance (sensitivity, resolution, and accuracy) of each technique will also be briefly discussed.

4.1. MPI–MRI dual-modal imaging

MPI is a new imaging technique, which directly visualizes the spatial distribution of magnetic nanoparticles with several advantageous features.[5,40,41] First, MPI is quantitative because the signal intensity of MPI is directly proportional to the concentration of magnetic nanoparticles. Second, MPI has no background signals because biological tissues and organs are diamagnetic and, thus, free from image ambiguities. Third, MPI can be used for real-time imaging because it has a fast imaging speed comparable to optical imaging and US imaging. Moreover, MPI is considered safe and has no penetration depth limit because it utilizes magnetic fields to perform the imaging measurements. Since the concept of MPI was introduced in 2005,[5] this technique has been tested for cardiovascular system imaging, cell tracking, and diseases diagnosis. Currently, MPI in combination with MRI makes it possible to obtain sensitive and accurate information about nanoparticle location, while at the same time achieving high resolution anatomical imaging.

4.1.1. Basic principles of MPI. Under an external magnetic field (H), the magnetic moments of the nanoparticles are aligned parallel with the direction of the external magnetic field, resulting in a magnetization vector (M).[5,40,41] When H becomes sufficiently large, M becomes saturated. The relationship between H and M is non-linear, and MPI utilizes this non-linear magnetization of magnetic nanoparticles to produce the MPI signal. When the magnetic nanoparticles are exposed to an oscillating external magnetic field (also called a modulation field), the magnetic nanoparticles emit a time-dependent magnetization $M(t)$, which includes a drive frequency ($1f_1$) and a series of harmonic frequencies (Fig. 7a).[5] These electromagnetic signals are detected and converted into MPI images. However, when magnetic nanoparticles are exposed to strong

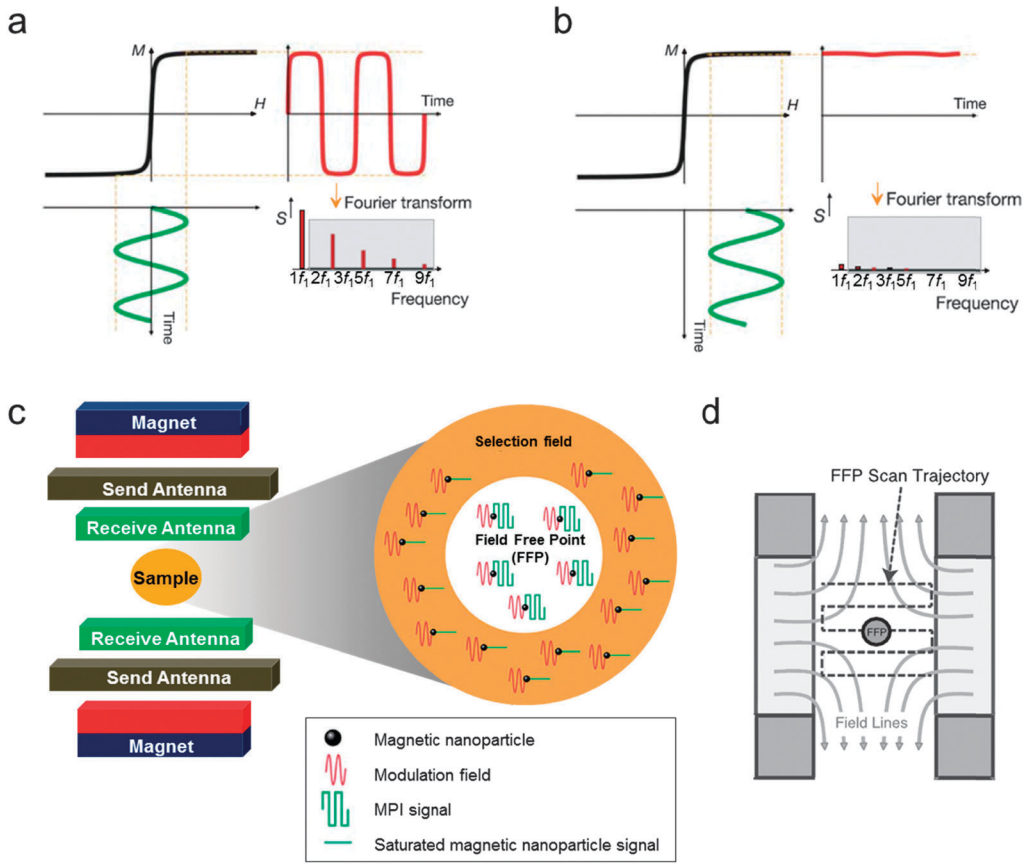

Fig. 7 Basics of magnetic particle imaging (MPI). (a and b) Response of the magnetic nanoparticles to an external magnetic field. (a) When the modulation field (*H*, green curve) with a frequency of f_1 is applied, time-dependent magnetization (*M*(*t*), red curve) and harmonics frequencies (*S*, red bars) are induced. The harmonics indicated by the grey box are used for MPI image generation. (b) When an additional time-independent external magnetic field (selection field) is added, the magnetic nanoparticles are magnetically saturated and the magnetization of the nanoparticles is not changed by the modulation field, resulting in neither *M*(*t*) nor *S*. (c) Schematic of the MPI instrument and the MPI signal generation. The magnet generates a selection field (orange region) that has a field-free point (FFP, white region) in the center. In addition, the send antenna creates a modulation field to magnetize the nanoparticles. The MPI signal produced by the magnetic nanoparticles located in the FFP is detected by the receive antenna. (d) Illustration of FFP raster scanning. (a and b) Reprinted with permission from Macmillan Publishers Ltd: ref. 5, copyright 2005. (c) Reproduced from ref. 41. (d) Reproduced from ref. 40 by permission of John Wiley & Sons Ltd.

external magnetic fields, they are magnetically saturated and do not respond to the applied modulation field, resulting in the suppression of the harmonic frequency generation (Fig. 7b). Based on this phenomenon, the MPI signal can be acquired in a spatially selective manner (Fig. 7c).[41] The spatial selectivity is achieved by applying an additional strong static magnetic field (also known as the selection field) that is high enough to saturate the magnetization of the magnetic nanoparticles. At the center of the selection field, there is a region, called a field-free point (FFP), where the magnetic field is zero. In this way, only magnetic nanoparticles located in the FFP can generate an MPI signal. To create an entire MPI image, FFP is raster scanned until every point in the field-of-view has been examined (Fig. 7d).[40]

4.1.2. Magnetic nanoparticles as MPI tracers. The optimization of magnetic nanoparticles is critical because the performance (sensitivity and resolution) of MPI depends on the physicochemical properties of the magnetic nanoparticles. The magnetization response of magnetic nanoparticles to a modulating field largely depends on magnetic relaxation properties of nanoparticles.[41] The magnetic relaxation process is a combined result of Néel and Brownian relaxation processes. The Néel relaxation time (τ_N), the Brownian relaxation time (τ_B), and the total relaxation time (τ) are described in eqn (3)–(5)

$$\tau_N = \tau_0 \exp\left(\frac{K_A V}{k_B T}\right) \quad (3)$$

$$\tau_B = \frac{3\eta V_H}{k_B T} \quad (4)$$

$$\tau = \frac{\tau_B \tau_N}{\tau_B + \tau_N} \quad (5)$$

where K_A is the anisotropy constant, V is the volume of the nanoparticle, k_B is the Boltzmann constant, T is the temperature, η is the fluid viscosity, and V_H is the hydrodynamic volume.[41] Therefore, it is possible to control the magnetic relaxation and optimize the magnetization response of the nanoparticles by modulation of the volume (V), anisotropy (K_A), and fluidity (η).

Currently, the development of MPI tracers is still in its early stages and mainly focuses on the nanoparticle size effects on the MPI sensitivity and the resolution enhancement. Commercial iron oxide nanoparticles (Resovist®; core size = 4–6 nm, size distribution (σ) = 0.37) are tested (Fig. 8a), and the *in vivo* biodistribution of Resovist® is successfully visualized using MPI–MRI dual-modal imaging (Fig. 8b).[40,42] A simulation study suggests that monodisperse 30 nm iron oxide nanoparticles can increase the MPI signal by 30-fold compared with Resovist®.[5,42] Recently, several experimental studies have shown nanoparticle size effects. By synthesizing 20 nm Fe_3O_4 nanoparticles, it is possible to achieve a *ca.* 1.2-fold higher spatial resolution and a 4-fold higher sensitivity compared with Resovist® using an oscillating magnetic field of 25 kHz.[42] Additionally, iron oxide nanoparticle-micelles (ION-Micelles), where 25 nm Fe_3O_4 nanoparticles are encapsulated in lipidic micelles (Fig. 8c), show an approximately 6 times higher MPI signal than the commercial iron oxide nanoparticles (Endorem®, Resovist®, and Sinerem®) in 25 kHz magnetic particle spectrometer measurements (Fig. 8d).[43] The MPI signal can also be increased by clustering magnetic nanoparticles. Typically, multicore magnetic nanoparticles, which are clusters of small single iron oxide nanoparticles, show an MPI performance exceeding that of single nanoparticles.[44] These examples clearly demonstrate the relationship between the quality of the MPI image and the size of the magnetic nanoparticle tracers. Additional studies on the other factors, including the magnetic core structures, compositions, and surface chemistry for molecular imaging capabilities, are necessary for the development of high performance nanoparticles for MPI–MRI dual-modal imaging.

4.2. Magnetic nanoparticle-assisted multi-modal ultrasound imaging

Ultrasound (US) imaging is one of the most widely used biomedical imaging techniques in clinical practice, such as angiography, echocardiography, and metastatic tumor detection.[45] US has several advantages, including real-time imaging capability, high resolution, reasonable penetration depth, cost effectiveness, and portability. However, conventional US has a drawback due to its limited sensitivity. US contrast agents, such as liposomes, perfluorocarbon droplets, and microbubbles, have been examined, but their contrast enhancement effects are still insufficient to clearly detect subtle biological differences in pathology.[46] Recent reports suggest that the sensitivity of US can also be improved by magnetic nanoparticles. This magnetic nanoparticle-assisted multi-modal US imaging is promising for visualizing biological events at the cellular and molecular level in real time. Two representative multi-modal US

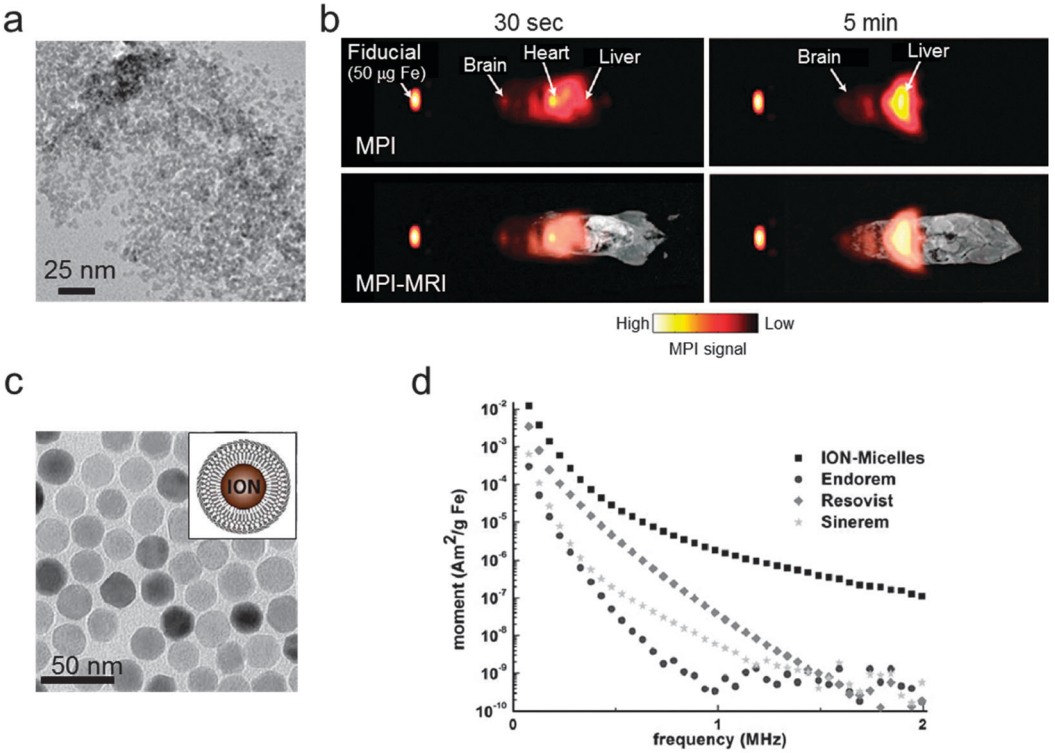

Fig. 8 MPI–MRI dual-mode imaging agents. (a) TEM image of Resovist®. (b) Full-body MPI–MRI dual-modal imaging using Resovist® for the *in vivo* biodistribution study. Resovist® is observed in the brain, heart, and liver 30 sec after injection, followed by significant accumulation in the liver after 5 min. (c) TEM image and schematic illustration of ION-Micelles. (d) The MPI signal generating capabilities of the various iron oxide nanoparticles (ION-Micelles, Endorem®, Resovist®, and Sinerem®) as shown in the plot of the magnetic moment *vs.* the oscillating magnetic field frequency. The higher magnetic moment of ION-Micelles compared with the other nanoparticles over the entire frequency range allows for a stronger MPI signal. (a) Reprinted with permission from ref. 42. Copyright 2012, American Institute of Physics. (b) Reproduced from ref. 40 by permission of John Wiley & Sons Ltd. (c and d) Reproduced with permission from ref. 43. Copyright 2013 Starmans *et al.*

imaging techniques have been introduced: (i) magneto-motive ultrasound (MMUS)–US and (ii) magneto-photoacoustic (MPA)–US.

4.2.1. MMUS–US dual-modal imaging. In MMUS imaging, a focused high intensity pulsed magnetic field is applied to the magnetic nanoparticles and their induced motion (*i.e.* displacement) is monitored using US imaging (Fig. 9a).[6] Thus, it is possible to determine the distribution of the magnetic nanoparticles in biological systems. Because most biological components (*e.g.* tissues and organs) are diamagnetic, they are silent under an external magnetic field.[46] Due to their large magnetic susceptibility (χ), magnetic nanoparticles respond readily to magnetic fields and move towards the magnetic field. However, during the displacement, the nanoparticles inevitably experience tissue resistance (force), which acts against the magnetically induced displacement. Due to these two forces (magneto-motive force and tissue resistance force), magnetic nanoparticles induce vibrations that can be detected using ultrasound-based motion tracking techniques. In a combined image of MMUS and US, only the presence of magnetic nanoparticles is visualized using MMUS along with the anatomical information provided by the US. Fig. 9b shows MMUS–US dual-modal imaging of sentinel lymph nodes (SLN).[47] The presence of 11 nm Fe_3O_4 nanoparticles in the SLN is clearly shown by the color-coded MMUS signal superimposed on the US image (Fig. 9b).

The relationship between the MMUS signal intensity and the susceptibility of the magnetic nanoparticles is shown in eqn (6)

$$\text{MMUS signal} \propto F_m = \frac{V_{np} f_m \chi_{np}}{\mu_0} B_z \frac{\delta B_z}{\delta_z} \quad (6)$$

where F_m is the magneto-motive force, V_{np} is the total volume of the nanoparticle, f_m is the volumetric magnetic fraction, χ_{np} is

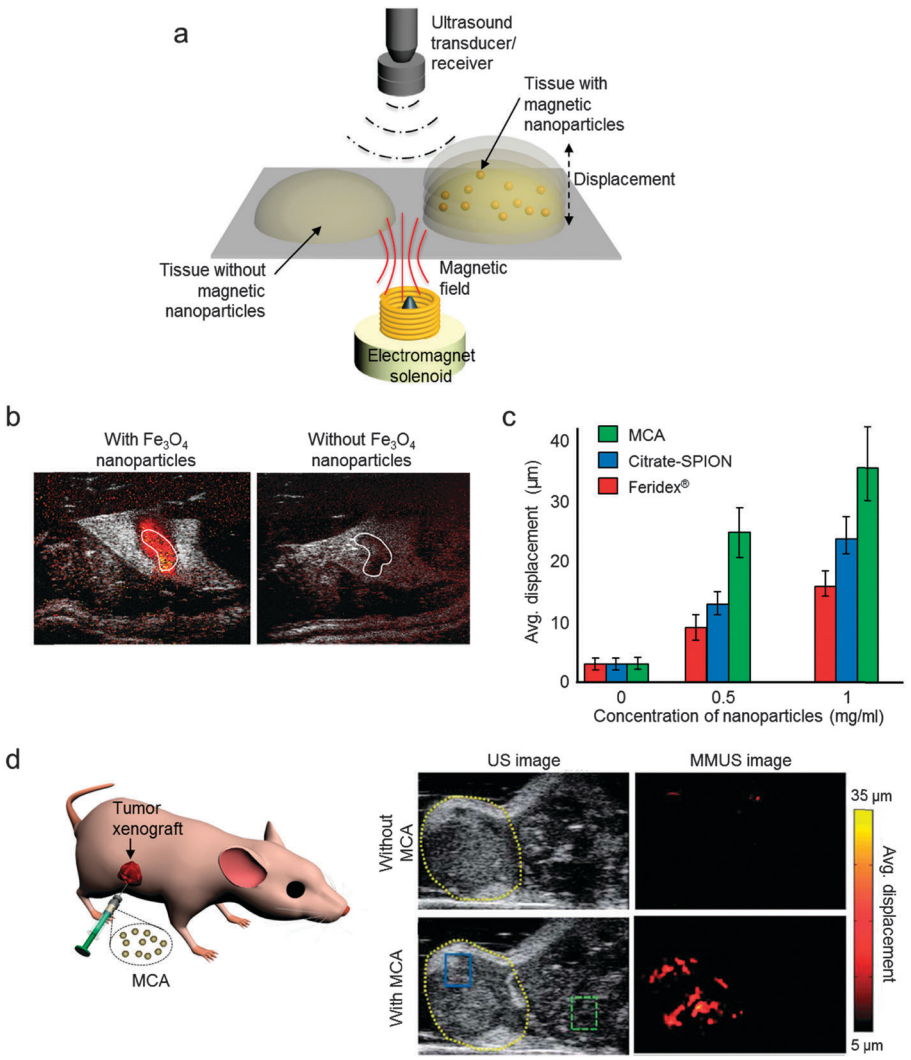

Fig. 9 Magneto-motive ultrasound (MMUS)–US dual-modal imaging. (a) Magnetically induced displacement of the tissue embedded with magnetic nanoparticles generates a MMUS signal, which is detected using an ultrasound receiver. (b) The MMUS–US dual-modal imaging of sentinel lymph nodes (SNL, white solid line). In the presence of Fe_3O_4 nanoparticles, the SNL is shown with color-coded MMUS signal, while the SNL without Fe_3O_4 shows no MMUS signal. (c) Comparisons of the MMUS signals from various magnetic nanoparticles. The MMUS signal of MCA (15 nm Zn-doped ferrite nanoparticle) is *ca.* 2–3-fold higher than that of citrate-SPION and Feridex®. (d) *In vivo* US and MMUS images of a mouse with a tumor xenograft. Upon injection of MCA, MMUS signals clearly represent the tumor location marked by yellow dashed lines. (a, c, and d) Reproduced from ref. 6. (b) © [2014] IEEE. Reprinted with permission from ref. 47.

the volume magnetic susceptibility of the magnetic nanoparticle, and B_z is the magnetic excitation flux density.[46] Because the MMUS signal is directly proportional to χ of the magnetic nanoparticles, it is possible to enhance the sensitivity of MMUS by developing nanoparticles with higher magnetic susceptibilities. Recently, high performance magneto-active MMUS contrast agents (MCAs) are reported.[6] MCAs are composed of dextran-coated 15 nm, Zn-doped ferrite ($(Zn_{0.4}Fe_{0.6})Fe_2O_4$) nanoparticles. In phantom experiments, MCAs exhibit a signal enhancement of 2-fold and 3-fold compared with 7.5 nm Fe_3O_4 nanoparticles and Feridex®, respectively (Fig. 9c). Using the high MMUS signal, the imaging of MCAs located in xenograft tumors is successfully demonstrated (Fig. 9d). Although it is still in the primitive stages, MMUS–US dual-modal imaging has the potential to be a new imaging approach for cellular and molecular level dynamic imaging such as lymph node metastasis detection, stem cell tracking, and drug delivery monitoring. Furthermore, because the magnetically induced motion of magnetic nanoparticles is affected by the mechanical environments of biological tissues, MMUS–US can be useful for non-invasive assessment of the viscoelastic property of soft tissues; this property is one of the indicators in the determination of tissue abnormality and regeneration.[46]

4.2.2. MPA–US dual-modal imaging. In photoacoustic (PA) imaging, tissues absorb laser light and thermo-elastically expand, generating ultrasound waves.[48] This ultrasound is detected using a transducer that converts acoustic waves into electric signals, which are further processed to produce a PA image. Because many parts of PA imaging instrumentation can be shared with US, PA can be easily combined with US. In PA–US dual-modal imaging, PA enables visualization of targets with relatively high contrast, while US provides morphological details of the anatomy. The PA–US dual imaging can be useful for melanoma imaging, angiography, and brain imaging, where contrasts originate from endogenous chromophores (*e.g.* melanin, hemoglobin, and lipids) or exogenous PA contrast agents (*e.g.* NIR-absorbing chemical dyes and gold nanoparticles).[49] However, PA–US dual-modal imaging occasionally suffers from ambiguities arising from photoacoustic background signals, which are frequently generated by endogenous photoabsorbers within tissues (Fig. 10a).

Recently, the combination of PA with magnetic nanoparticles, so-called magneto-PA (MPA), is reported as an approach to enhance the quality of PA–US dual-modal imaging.[7] When a pulsed external magnetic field is applied during PA image acquisition, the magnetic nanoparticles create a vibrating motion while non-magnetic endogenous photoabsorbers remain still. By detecting the motion of the nanoparticles, the PA signals from the nanoparticles can be distinguished from the background (Fig. 10b).[7] This background elimination capability of MPA is demonstrated using 25 nm Fe_3O_4 nanoparticles and magnetic-gold core–shell nanoparticles (Fig. 10c). In the phantom experiments, both the magnetic nanoparticles and the magnetic-gold core–shell nanoparticles are successfully differentiated from gold nanorods, which are used as a control for the background signal (Fig. 10d). Another example of magnetic nanoparticle-aided PA imaging utilizes the principle of magnetic nanoparticle clustering (Fig. 11a and b).[50] Compared with single magnetic nanoparticles, clustered magnetic nanoparticles show a higher PA signal than the background signal (Fig. 11b). Based on this principle, magnetic nanoparticle-labeled tumor cells under flow conditions are successfully captured and further

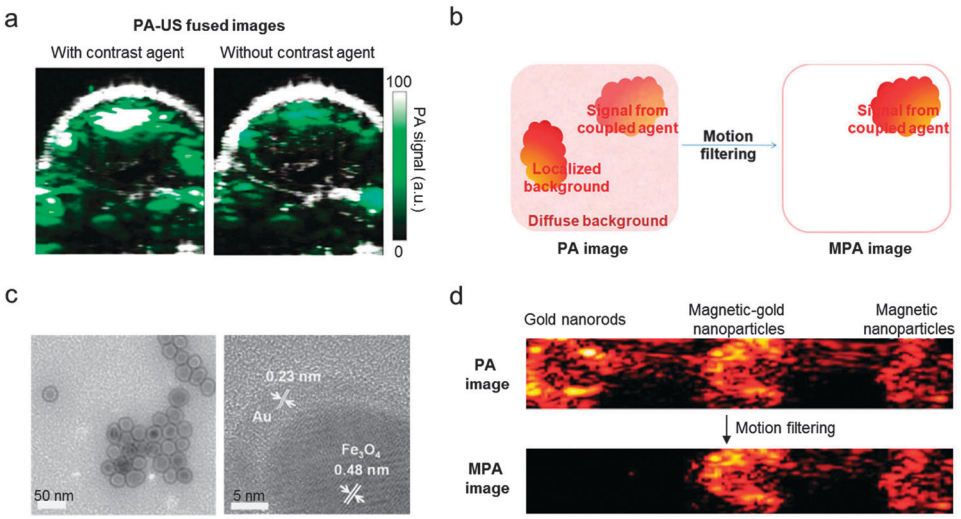

Fig. 10 Photoacoustic (PA) imaging accuracy enhancement *via* magneto-photoacoustic (MPA) imaging. (a) Conventional PA–US dual-modal imaging of tumors in a mouse using the PA contrast agent shows an increase of the PA signal (green). Non-negligible PA signals, which originate from background photoacoustic absorbers, are also observed in PA–US image without a contrast agent. (b) Schematic illustration of the background signal elimination *via* a motion filtering process. Only magnetic nanoparticle-based imaging agents that respond to a pulsed magnetic field can be distinguished from the background photoacoustic absorbers. (c) TEM images of the magnetic-gold nanoparticles. (d) Magnetic-gold nanoparticles and magnetic nanoparticles show strong MPA signals, while the signals from the gold nanorods that mimic the background is completely eliminated. (a) Reprinted with permission from ref. 49. Copyright 2010 American Chemical Society. (b–d) Reprinted with permission from Macmillan Publishers Ltd: ref. 7, copyright 2010.

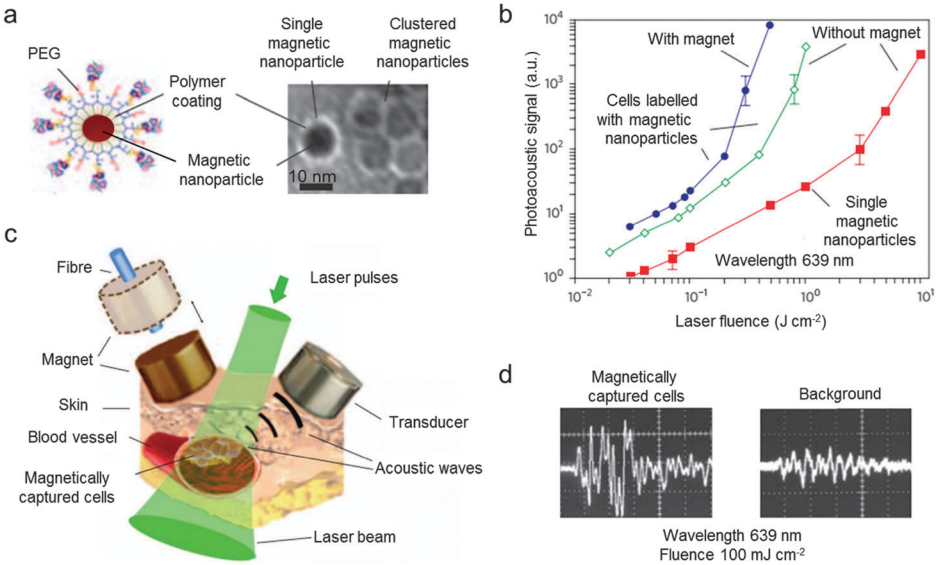

Fig. 11 Magnetic nanoparticle-assisted photoacoustic (PA) imaging. (a) Schematic illustration of a polymer-coated magnetic nanoparticle and the TEM image of single and clustered magnetic nanoparticles. (b) Comparison of the photoacoustic signals of cells labeled with clustered magnetic nanoparticles (blue), cells labeled with single magnetic nanoparticles (green), and single magnetic nanoparticles (red). The higher PA signal of the clustered magnetic nanoparticles over the single nanoparticles is observed. (c) Illustration of magnetic cell capturing and the PA imaging setup. (d) The magnetically captured cells show a strong PA signal than the background. Reprinted with permission from Macmillan Publishers Ltd: ref. 50, copyright 2009.

detected using PA imaging (Fig. 11c and d). These cell capturing and PA signal boosting capabilities of magnetic nanoparticles are further utilized in the detection of tumor cells circulating *in vivo*, which are some of the important biomarkers of cancer metastasis.

5. Conclusions and outlook

In this review, we discussed recent advances of magnetic nanoparticles for various biomedical imaging modalities. Metal ferrite nanoparticles can be used as either T_1 or T_2 MRI contrast agents. By controlling the magnetism of the nanoparticles *via* size, composition, and shape, the MRI contrast effects can be enhanced to achieve highly sensitive MRI. Complementary combinations of various types of materials (*e.g.* fluorescent molecules and radioisotopes) provide nanoparticles with multi-modal imaging capabilities. Moreover, magnetic nanoparticles have become a platform for the new types of contrast agents used in emerging imaging technologies such as MPI, MMUS, and MPA. These magnetic nanoparticle-based multimodal imaging approaches hold new promise to secure enhanced imaging sensitivity and accuracy for a better understanding of biological systems and accurate imaging of biological targets.

Acknowledgements

This work was supported by the National Creative Research Initiative (2010-0018286) and the Korea Healthcare Technology R&D Project, Ministry for Health & Welfare Affairs (HI08C2149). We thank Dr Dongwon Yoo for helpful discussion.

References

1 E. T. Ahrens and J. W. M. Bulte, *Nat. Rev. Immunol.*, 2013, **13**, 755–763.
2 D.-E. Lee, H. Koo, I.-C. Sun, J. H. Ryu, K. Kim and I. C. Kwon, *Chem. Soc. Rev.*, 2012, **41**, 2656–2672.
3 J. Cheon and J.-H. Lee, *Acc. Chem. Res.*, 2008, **41**, 1630–1640.
4 H. B. Na, I. C. Song and T. Hyeon, *Adv. Mater.*, 2009, **21**, 2133–2148.
5 B. Gleich and J. Weizenecker, *Nature*, 2005, **435**, 1214–1217.
6 M. Mehrmohammadi, T.-H. Shin, M. Qu, P. Kruizinga, R. L. Truby, J.-H. Lee, J. Cheon and S. Y. Emelianov, *Nanoscale*, 2013, **5**, 11179–11186.
7 Y. Jin, C. Jia, S.-W. Huang, M. O'Donnell and X. Gao, *Nat. Commun.*, 2010, **1**, 41–48.
8 C. P. Slichter, *Principles of Magnetic Resonance*, Springer, New York, 3rd edn, 1990.
9 S. Tong, S. Hou, Z. Zheng, J. Zhou and G. Bao, *Nano Lett.*, 2010, **10**, 4607–4613.
10 B. H. Kim, N. Lee, H. Kim, K. An, Y. I. Park, Y. Choi, K. Shin, Y. Lee, S. G. Kwon, H. B. Na, J.-G. Park, T.-Y. Ahn, Y.-W. Kim, W. K. Moon, S. H. Choi and T. Hyeon, *J. Am. Chem. Soc.*, 2011, **133**, 12624–12631.
11 A. Roch, R. N. Muller and P. Gillis, *J. Chem. Phys.*, 1999, **110**, 5403–5411.
12 R. A. Brooks, *Magn. Reson. Med.*, 2002, **47**, 388–391.
13 Y.-w. Jun, Y.-M. Huh, J.-s. Choi, J.-H. Lee, H.-T. Song, S. Kim, S. Yoon, K.-S. Kim, J.-S. Shin, J.-S. Suh and J. Cheon, *J. Am. Chem. Soc.*, 2005, **127**, 5732–5733.
14 J.-s. Choi, J.-H. Lee, T.-H. Shin, H.-T. Song, E. Y. Kim and J. Cheon, *J. Am. Chem. Soc.*, 2010, **132**, 11015–11017.

15 S. Balasubramaniam, S. Kayandan, Y.-N. Lin, D. F. Kelly, M. J. House, R. C. Woodward, T. G. St. Pierre, J. S. Riffle and R. M. Davis, *Langmuir*, 2014, **30**, 1580–1587.
16 J.-H. Lee, Y.-w. Jun, S.-I. Yeon, J.-S. Shin and J. Cheon, *Angew. Chem., Int. Ed.*, 2006, **45**, 8160–8162.
17 J. M. Perez, L. Josephson, T. O'Loughlin, D. Hogemann and R. Weissleder, *Nat. Biotechnol.*, 2002, **20**, 816–820.
18 J. B. Haun, T.-J. Yoon, H. Lee and R. Weissleder, *Wiley Interdiscip. Rev.: Nanomed. Nanobiotechnol.*, 2010, **2**, 291–304.
19 L. Sandiford, A. Phinikaridou, A. Protti, L. K. Meszaros, X. Cui, Y. Yan, G. Frodsham, P. A. Williamson, N. Gaddum, R. M. Botnar, P. J. Blower, M. A. Green and R. T. M. de Rosales, *ACS Nano*, 2012, **7**, 500–512.
20 J.-H. Lee, Y.-M. Huh, Y.-w. Jun, J.-w. Seo, J.-t. Jang, H.-T. Song, S. Kim, E.-J. Cho, H.-G. Yoon, J.-S. Suh and J. Cheon, *Nat. Med.*, 2007, **13**, 95–99.
21 J.-t. Jang, H. Nah, J.-H. Lee, S. H. Moon, M. G. Kim and J. Cheon, *Angew. Chem., Int. Ed.*, 2009, **48**, 1234–1238.
22 Z. Zhou, L. Wang, X. Chi, J. Bao, L. Yang, W. Zhao, Z. Chen, X. Wang, X. Chen and J. Gao, *ACS Nano*, 2013, **7**, 3287–3296.
23 J. W. M. Bulte and D. L. Kraitchman, *NMR Biomed.*, 2004, **17**, 484–499.
24 J. G. Penfield and R. F. Reilly, *Nat. Clin. Pract. Nephrol.*, 2007, **3**, 654–668.
25 Z. Zhao, Z. Zhou, J. Bao, Z. Wang, J. Hu, X. Chi, K. Ni, R. Wang, X. Chen, Z. Chen and J. Gao, *Nat. Commun.*, 2013, **4**, 2266–2272.
26 Z. Zhou, Z. Zhao, H. Zhang, Z. Wang, X. Chen, R. Wang, Z. Chen and J. Gao, *ACS Nano*, 2014, **8**, 7976–7985.
27 K. H. Bae, Y. B. Kim, Y. Lee, J. Hwang, H. Park and T. G. Park, *Bioconjugate Chem.*, 2010, **21**, 505–512.
28 Z. Zhou, D. Huang, J. Bao, Q. Chen, G. Liu, Z. Chen, X. Chen and J. Gao, *Adv. Mater.*, 2012, **24**, 6223–6228.
29 G. Huang, H. Li, J. Chen, Z. Zhao, L. Yang, X. Chi, Z. Chen, X. Wang and J. Gao, *Nanoscale*, 2014, **6**, 10404–10412.
30 T.-H. Shin, J.-s. Choi, S. Yun, I.-S. Kim, H.-T. Song, Y. Kim, K. I. Park and J. Cheon, *ACS Nano*, 2014, **8**, 3393–3401.
31 L. Josephson, M. F. Kircher, U. Mahmood, Y. Tang and R. Weissleder, *Bioconjugate Chem.*, 2002, **13**, 554–560.
32 H. Lee, M. K. Yu, S. Park, S. Moon, J. J. Min, Y. Y. Jeong, H.-W. Kang and S. Jon, *J. Am. Chem. Soc.*, 2007, **129**, 12739–12745.
33 E. S. Shibu, K. Ono, S. Sugino, A. Nishioka, A. Yasuda, Y. Shigeri, S.-i. Wakida, M. Sawada and V. Biju, *ACS Nano*, 2013, **7**, 9851–9859.
34 L. Cheng, K. Yang, Y. Li, J. Chen, C. Wang, M. Shao, S.-T. Lee and Z. Liu, *Angew. Chem., Int. Ed.*, 2011, **50**, 7385–7390.
35 H. Ow, D. R. Larson, M. Srivastava, B. A. Baird, W. W. Webb and U. Wiesner, *Nano Lett.*, 2004, **5**, 113–117.
36 J.-s. Choi, J. C. Park, H. Nah, S. Woo, J. Oh, K. M. Kim, G. J. Cheon, Y. Chang, J. Yoo and J. Cheon, *Angew. Chem., Int. Ed.*, 2008, **47**, 6259–6262.
37 H.-Y. Lee, Z. Li, K. Chen, A. R. Hsu, C. Xu, J. Xie, S. Sun and X. Chen, *J. Nucl. Med.*, 2008, **49**, 1371–1379.
38 R. Torres Martin de Rosales, R. Tavaré, R. L. Paul, M. Jauregui-Osoro, A. Protti, A. Glaria, G. Varma, I. Szanda and P. J. Blower, *Angew. Chem., Int. Ed.*, 2011, **50**, 5509–5513.
39 F. Chen, P. A. Ellison, C. M. Lewis, H. Hong, Y. Zhang, S. Shi, R. Hernandez, M. E. Meyerand, T. E. Barnhart and W. Cai, *Angew. Chem., Int. Ed.*, 2013, **52**, 13319–13323.
40 P. W. Goodwill, E. U. Saritas, L. R. Croft, T. N. Kim, K. M. Krishnan, D. V. Schaffer and S. M. Conolly, *Adv. Mater.*, 2012, **24**, 3870–3877.
41 M. H. Pablico-Lansigan, S. F. Situ and A. C. S. Samia, *Nanoscale*, 2013, **5**, 4040–4055.
42 R. M. Ferguson, A. P. Khandhar and K. M. Krishnan, *J. Appl. Phys.*, 2012, **111**, 07B318.
43 L. W. E. Starmans, D. Burdinski, N. P. M. Haex, R. P. M. Moonen, G. J. Strijkers, K. Nicolay and H. Grüll, *PLoS One*, 2013, **8**, e57335.
44 D. Eberbeck, F. Wiekhorst, S. Wagner and L. Trahms, *Appl. Phys. Lett.*, 2011, **98**, 182502.
45 T. L. Szabo, *Diagnostic Ultrasound Imaging: Inside Out*, Elsevier Academic Press, San Diego, 2004.
46 M. Mehrmohammadi, J. Oh, S. Mallidi and S. Y. Emelianov, *Mol. Imaging*, 2011, **10**, 102–110.
47 M. Evertsson, P. Kjellman, M. Cinthio, S. Fredriksson, R. in't Zandt, H. Persson and T. Jansson, *IEEE Trans. Ultrason., Ferroelectr., Freq. Control.*, 2014, **61**, 1276–1283.
48 L. V. Wang and S. Hu, *Science*, 2012, **335**, 1458–1462.
49 A. d. l. Zerda, Z. Liu, S. Bodapati, R. Teed, S. Vaithilingam, B. T. Khuri-Yakub, X. Chen, H. Dai and S. S. Gambhir, *Nano Lett.*, 2010, **10**, 2168–2172.
50 E. I. Galanzha, E. V. Shashkov, T. Kelly, J.-W. Kim, L. Yang and V. P. Zharov, *Nat. Nanotechnol.*, 2009, **4**, 855–860.

